The Journal of Experimental Biology 205, 3783–3792 (2002)
Printed in Great Britain © The Company of Biologists Limited
JEB4333

Rotational lift: something different or more of the same?

Jeffrey A. Walker

Department of Biology, University of Southern Maine, 96 Falmouth St, Portland, ME 04103, USA

(e-mail: walker@usm.maine.edu)

Accepted 16 September 2002

Summary

This paper addresses the question, do the rotational forces in the hovering fruit fly *Drosophila melanogaster* reflect something different (the Magnus effect) or more of the same (circulatory-and-attached-vortex force)? The results of an unsteady blade-element model using empirically derived force coefficients from translating (root-oscillating) wings are compared with recent results derived from both the measured forces on a dynamically scaled *Drosophila* wing and the computational fluid dynamic (CFD)-modeled forces on a virtual *Drosophila* wing. The behavior of the forces in all three models during wing rotation supports the hypothesis that rotational lift is not a novel aerodynamic mechanism but is caused by the same fluid-dynamic mechanism that occurs during wing translation. A comparison of the unsteady model with a quasi-steady model that employs empirically derived rotational coefficients further supports the hypothesis that rotational forces are more of the same. Finally, the overall similarity of the results between the unsteady model, the physical wing model and the CFD model suggests that the unsteady model can be used to explore the performance consequences of kinematic variation and to investigate locomotor control in freely moving animals.

Key words: unsteady aerodynamics, rotational circulation, delayed stall, Magnus effect, attached vortex lift, hovering, *Drosophila* flight.

Introduction

Motor-driven, scaled-up model wings of a hovering hawkmoth, *Manduca sexta* L., and fruit fly, *Drosophila melanogaster* (Meigen 1830), have allowed tremendous progress in our understanding of the flight forces on hovering insect wings. Visualization of the flow past the *Manduca* model wings confirmed the expectation (Ellington, 1984; Dickinson and Götz, 1993) that an attached leading-edge vortex augments flight forces during the translation phase of wing movement and showed that a spanwise flow stabilized the vortex and prevented its shedding into the wake (Van den Berg and Ellington, 1997a,b).

Measured forces on the model wings of *Drosophila* support previous work showing that a large portion of the lift impulse is generated during stroke reversals (Dickinson et al., 1999). These model *Drosophila* experiments showed two force peaks during stroke reversal. One peak occurred while the wing was rapidly pitching about a spanwise axis, and the timing and sign of this peak was a function of the timing of wing rotation. Because of this behavior, Dickinson et al. (1999) argued that the rotation of the wing adds a rotational circulation component to the total circulation and that the associated force component is similar to the Magnus force occurring on translating and rotating cylinders and spheres. The second peak occurs immediately after stroke reversal and is independent of the timing of wing rotation. This behavior suggested to Dickinson et al. (1999) that the aerodynamic force is augmented because of an interaction with the wake shed by the previous stroke. These interpretations of the rotational forces have been challenged by recent computational fluid dynamic (CFD) results suggesting that the rotation-dependent peak can be explained by the rapid generation of strong vorticity due to wing rotation, while the rotation-independent peak can be explained by the acceleration reaction (the reaction to accelerating an added mass of fluid; Sun and Tang, 2002).

The present study explores the nature of the rotation-dependent peak and how it can be modeled. The theoretical force (F), per unit span, on a thin-airfoil in translation and rotation at low angles of attack is a function of the superposition of four circulatory components:

$$F = \rho U(\Gamma_t + \Gamma_h + \Gamma_r + \Gamma_M), \quad (1)$$

where ρ is fluid density, U is fluid velocity, Γ_t is the translational circulation due to the wing being attached to a translating body, Γ_h is the heaving circulation due to the wing actively or passively oscillating, Γ_r is the rotational circulation due to the wing rotating around a spanwise axis, and Γ_M is the Magnus circulation (*sensu stricto*), which is also due to wing rotation (Fung, 1993). Γ_t, Γ_h and Γ_r arise because the corresponding kinematic components (translation, heaving and rotation, respectively) create an incident flow at a finite angle (α') with the wing section. The presence of a finite angle between the wing section and incident flow distorts the boundary layer, creating an asymmetry in the speed of flow over the upper and lower surface of the wing section. Γ_M

differs from the other circulatory components because it is independent of α'.

The distortion and resulting normal (lift) force on a pitched wing in a uniform flow (in which case, only Γ_t applies) is similar to the Magnus effect – the distortion of the boundary layer and resulting lift that occur on a cylinder or sphere that is both translating and rotating around an axis normal to the translation. The force component due to Γ_t is, therefore, a Magnus-like force but is not the Magnus-like force discussed by Dickinson et al. (1999). Flapping and rotating wings in a uniform flow will distort the boundary layer similarly (again, because of their influence on α'). The force components due to Γ_h and Γ_r are, therefore, Magnus-like forces, but the component due to Γ_h is also not the Magnus-like force discussed by Dickinson et al. (1999). The force component due to Γ_r arises from the rotational component of the wing's motion to the incident flow and the resulting α' (see below) and, in this sense, it is really no different from the force components due to Γ_t and Γ_h. Because the Γ_r component is due to wing rotation, and the dynamics of the associated force partially resemble the Magnus effect on rotating cylinders, it is this force component that Dickinson et al. (1999) refer to as Magnus-like. The force component due to Γ_M is similar to that due to Γ_r in that it is dependent on wing rotation but differs from the Γ_r component in that it is independent of the angle of the incident flow. Because Γ_M is also independent of the chordwise center of the incident flow (in contrast to Γ_r), the force component due to Γ_M exactly resembles the Magnus effect on a rotating cylinder and it is this force that Sun and Tang (2002) refer to as the Magnus force. I refer to the combined force due to Γ_t, Γ_h and Γ_r as the circulatory-and-attached-vortex force (see below), and the force due to Γ_M as the Magnus force.

In this paper, I use a previously developed (Walker and Westneat, 2000), semi-empirical, unsteady blade-element (USBE) model to address the question, do the rotational forces in the hovering fruit fly reflect something different (Magnus circulation and corresponding Magnus force) or more of the same (circulatory-and-attached-vortex force)? The unsteady results are quite similar to the measured forces on the physical wing models and to CFD estimates of the flight forces, and the rotational forces are well modeled by unsteady coefficients measured on translating wings, which supports the hypothesis that forces occurring during wing rotation arise from the same fluid-dynamic mechanisms as forces occurring during wing translation (*viz* the circulatory-and-attached-vortex force and acceleration reaction).

Materials and methods

The unsteady blade-element model

A very general, semi-empirical, unsteady blade-element (USBE) model of the dynamics of a root-oscillating limb (wing or fin) was developed previously (Walker and Westneat, 2000). The model has two components; one due to added mass (acceleration reaction) and the other due to unsteady circulation and the influence of an attached vortex. The geometry of the incident flow and incident angle of attack in the USBE model is a large-angle generalization of Theodorsen's model of a wing in flutter (Theodorsen, 1935), which is described in detail by Fung (1993). The history of the Theodorsen and similar models and applications to insect flight are outlined by Zbikowski (2002). Applications of the Theodorsen model to the flapping flight of vertebrates are found in DeLaurier (1993) and Kamakoti et al. (2000). The unique feature of the USBE model is that empirical force coefficients measured from oscillating wings are used instead of theoretical coefficients based on the Theodorsen function or its modifications. Unsteady coefficients based on the Theodorsen function are not a function of time but are unsteady in that they are a function of the reduced frequency parameter. The raw coefficients used in this study are steady in both senses (although they are modified by the unsteady Wagner function). The Theodorsen coefficients are an approximation for low angles of incidence and attached flow. Consequently, the Theodorsen coefficients are not particularly useful for much of the wing stroke of a hovering *Drosophila* because the *Drosophila* stroke is characterized by incident angles that are much larger than the stall angle throughout much of the stroke cycle (Dickinson et al., 1999). One advantage of the empirically derived coefficients is that they explicitly account for the augmenting effect of an attached vortex when the wing is above the stall angle.

While the augmented circulatory force due to Γ_r was included in the model, Magnus-type forces due to Γ_M were not. Magnus forces have not been previously modeled in biological applications of flapping wings, but Fung (1993) suggests that these forces should contribute to the lift balance. The extended model below adds this Magnus force component. The simple kinematics of a *Drosophila* wing oscillating along a horizontal stroke plane allow the model to be greatly simplified. The full model is detailed by Walker and Westneat (2000).

The USBE model begins with a geometric description of wing kinematics. The wing has length (span), R, and is arbitrarily divided along its span into p elements with equal width: $dR=R/p$. The length-specific radial position is $\hat{r}=r/R$, where r is the distance from the wing base. In the following, the bracketed subscripts indicate that a variable is a function of time (t) and/or radial position along the wing span (r).

The azimuth position of the wing, $\gamma_{(t)}$, is the angle between the rotational axis of the wing and a horizontal vector directed posterior to the fly. In this coordinate system, $\gamma_{(t)}$ is 0° when the rotational axis is back against the body and 90° when it is perpendicular to the body axis. Following previous work, the wing does not oscillate with simple harmonic motion but instead rapidly accelerates to a constant angular velocity. The non-dimensional period of linear acceleration at each stroke reversal is $\Delta\hat{\tau}_t$ and the timing of the acceleration is symmetric about the point of stroke reversal.

The pitch of a wing chord, $\alpha_{(t)}$, is the angle between the wing chord and the flapping axis (which is normal to the stroke plane and, therefore, vertical for the hovering *Drosophila*) (Fig. 1). $\alpha_{(t)}$ is negative when the wing is pronated and is positive when

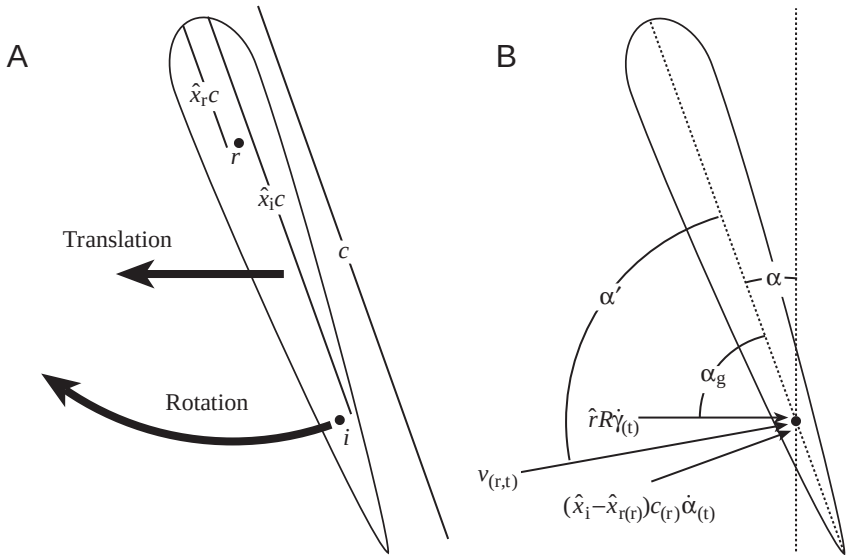

Fig. 1. Cross section of an airfoil illustrating geometry of the principal model parameters. (A) The arrows indicate that the wing is translating to the left due to root-flapping and rotating about the point *r* due to active supination or pronation. Point *i* is the location of the incident flow, which is illustrated in (B). The subscript (r) has been removed from $\hat{x}_r$, $\hat{x}_i$ and *c* for clarity. (B) The relevant flow velocity components due to root-flapping ($\hat{r}R\dot{\gamma}_{(t)}$) and wing rotation [$(\hat{x}_i-\hat{x}_{r(r)})c_{(r)}\dot{\alpha}_{(t)}$] and their resultant, $v_{(r,t)}$. Also illustrated are the wing pitch, α, the geometric attack angle, α_g, and the angle of incidence, α′, acting at the point *i* in (A).

the wing is supinated. The geometric angle of attack, $\alpha_{g(t)}$, is the angle of the wing chord relative to the stroke plane and is equal to $\pi/2+\alpha_{(t)}$ for the case of a horizontal stroke plane (Fig. 1). Again, the wing does not rotate with simple harmonic motion. The non-dimensional period of each rotational phase (there are two phases per stroke cycle) is $\Delta\hat{\tau}_r$, and the non-dimensional time difference between the mid-point of rotation and stroke reversal is $\hat{\tau}_f$ (Sane and Dickinson, 2001).

The normal, $v_{n(r,t)}$, and chordwise, $v_{x(r,t)}$, flow due to wing translation and rotation are:

$$v_{n(r,t)} = \dot{h}_{(r,t)}\cos(\alpha_{(t)}) + (\hat{x}_i - \hat{x}_{r(r)})c_{(r)}\dot{\alpha}_{(t)} \quad (2)$$

$$v_{x(r,t)} = \dot{h}_{(r,t)}\sin(\alpha_{(t)}). \quad (3)$$

These equations assume that the velocity component due to body translation is trivial, an assumption that is relaxed in the full model (Walker and Westneat, 2000). Equation 3 and the first component of Equation 2 are due to the wing element translating (due to flapping) with a speed, $\dot{h}_{(r,t)}=\hat{r}R\dot{\gamma}_{(t)}$. The second component of Equation 2 is due to the wing rotating around a spanwise axis located $\hat{x}_{r(r)}c_{(r)}$ from the leading edge and the chordwise center of incident flow located $\hat{x}_i c_{(r)}$ from the leading edge, where $\hat{x}_i$ and $\hat{x}_{r(r)}$ are percentage distances along the chord, and $c_{(r)}$ is chord length. It is important to note that $\hat{x}_{r(r)}$ is a function of wing shape and cannot be constant along the span. This is easily seen using, as an example, the distal wing chord on the wing illustrated by Sane and Dickinson (2002). If the rotational axis, $\hat{x}_o$, is 0.25, the entire distal element is posterior to the rotational axis, and the element-specific rotation axis, $\hat{x}_{r(r)}$, must be less than zero. The values of $\hat{x}_o$ used for each analysis are found in Table 1. The value of $\hat{x}_i$ must satisfy the boundary condition of tangent flow. For attached flow, $\hat{x}_i$ occurs at the three-quarter chord location (DeLaurier, 1993; Fung, 1993). While initial work on the root-oscillating *Drosophila* wing model indicated that $\hat{x}_i$=0.75 for separated flow (Dickinson et al., 1999), more detailed work has shown that $\hat{x}_i$ is a function of rotational velocity and can be as low as 0.57 (Sane and Dickinson, 2002). In the present study, a constant value of 0.75 was used, although future work could easily incorporate a $\hat{x}_i$ that is dependent on rotational velocity.

The angle of incidence, $\alpha'_{(r,t)}$, between the wing chord and the incident stream is $\pm\tan^{-1}(v_{n(r,t)}/v_{x(r,t)})$, where the ± takes the sign of $v_{x(r,t)}$ (Fig. 1). This angle is used to estimate the lift and drag coefficients (see below) and the components of the circulatory force normal to ($dF_{n(r,t)}$) and parallel with ($dF_{x(r,t)}$) the wing chord:

$$dF_{n(r,t)} = dL'_{(r,t)}\cos\alpha'_{(r,t)} + dD'_{(r,t)}\sin\alpha'_{(r,t)} \quad (4)$$

$$dF_{x(r,t)} = dL'_{(r,t)}\sin\alpha'_{(r,t)} - dD'_{(r,t)}\cos\alpha'_{(r,t)}. \quad (5)$$

$dL'_{(r,t)}$ and $dD'_{(r,t)}$, the components of the circulatory force normal to and parallel with the local stream, are:

$$dL'_{(r,t)} = \tfrac{1}{2}\rho v^2_{(r,t)}c_{(r)}\Phi_{(r,t)}C_{L(r,t)}dR \quad (6)$$

$$dD'_{(r,t)} = \tfrac{1}{2}\rho v^2_{(r,t)}c_{(r)}\Phi_{(r,t)}C_{D(r,t)}dR, \quad (7)$$

where

$$v^2_{(r,t)} = v^2_{n(r,t)} + v^2_{x(r,t)}. \quad (8)$$

$C_{L(r,t)}$ and $C_{D(r,t)}$ are empirically derived lift and drag coefficients measured from oscillating wings at a constant α′ (Dickinson et al., 1999). These coefficients reflect the augmenting effects of a stable, attached, leading-edge vortex on the downstream surface of the wing when α′ is above a threshold (approximately 13–15°). The additional component due to the attached vortex is known as the attached-vortex force (Kuethe and Chow, 1986). Despite the presence of the attached vortex, the measured coefficients on a root-oscillating wing at a constant angle of attack remain relatively stable for several chord lengths of travel (Dickinson et al., 1999; Usherwood and Ellington, 2002a) and can, therefore, be considered quasi-steady (Dickinson et al., 1999; Sane and Dickinson, 2002). It is important to note that the coefficients were measured following the influence of the initial, inertial peak and Wagner-effect trough (Dickinson et al., 1999). In

Table 1. *Kinematic variables for the physical wing model (PM) and virtual wing model (VM) comparisons*

Case	Source	Fig.	$\Delta\hat{\tau}_t$	$\Delta\hat{\tau}_r$	$\hat{\tau}_f$	$\hat{x}_o$	α_{down}	α_{up}
PM1	1	1	0.12	0.32	–0.08	0.2	–50	70
PM2	1	3	0.12	0.32	–0.08	0.2	–50	50
PM3	1	3	0.12	0.32	0.08	0.2	–50	50
VM1	2	6	0.24	0.32	–0.08	0.2	–50	50
VM2	2	6	0.105	0.32	–0.08	0.2	–50	50
VM3	2	11	0.24	0.32	0	0.2	–50	50
VM4	2	11	0.24	0.32	0.08	0.2	–50	50

Source 1, Dickinson et al., 1999; Source 2, Sun and Tang, 2002. Fig. refers to the figure in the source paper from which the force curves were digitized.

In PM1, PM2, VM1 and VM2, wing rotation is 'advanced' relative to stroke reversal. In PM3 and VM4, rotation is 'delayed'. In VM3, wing rotation is symmetric about stroke reversal.

$\Delta\hat{\tau}_t$ is the non-dimensional duration of wing translational velocity; $\Delta\hat{\tau}_r$ is the non-dimensional duration of wing rotation; $\hat{\tau}_f$ is the non-dimensional rotational timing parameter; $\hat{x}_o$ is the rotational axis; α_{down} and α_{up} are the pitch angles of the wing during the translation phase of the down and up strokes, respectively.

Equations 6 and 7, $\Phi_{(r,t)}$ is the Wagner function due to Garrick (Fung, 1993) and accounts for the interaction between the wing and the starting vortex at the beginning of a stroke. It is this function that effectively makes the coefficients in this model unsteady. The time-course of this wing-wake interaction effect is much longer than that due to wake capture (which is not included in the model). The vertical (lift) and horizontal (drag) force components on a blade element due to the circulatory-and-attached-vortex force are:

$$dL_{c(r,t)} = [dF_{n(r,t)}\cos(\alpha_{g(t)}) + dF_{x(r,t)}\sin(\alpha_{g(t)})] \quad (9)$$

$$dD_{c(r,t)} = [dF_{n(r,t)}\sin(\alpha_{g(t)}) + dF_{x(r,t)}\cos(\alpha_{g(t)})]\,. \quad (10)$$

Note that if the rotational component of the resultant stream were ignored, lift and drag could be estimated directly from Equations 6 and 7.

The added mass force, or acceleration reaction, normal to the wing element is:

$$dF_{a(r,t)} = \frac{\pi}{4}\rho c_{(r)}^2 \dot{v}_{n(r,t)} \beta_n dR\,, \quad (11)$$

where β_n is the added mass coefficient of the wing section (a value of 1.0 was used). $\hat{x}_i$=0.5 was used for the computation of $\dot{v}_{n(r,t)}$ (see Equation 2 above; DeLaurier, 1993; Fung, 1993). The vertical (lift) and horizontal (drag) components of $dF_{a(r,t)}$ are:

$$dL_{a(r,t)} = dF_{a(r,t)}\cos(\alpha_{g(t)}) \quad (12)$$

$$dD_{a(r,t)} = dF_{a(r,t)}\sin(\alpha_{g(t)})\,. \quad (13)$$

The acceleration reaction is an unsteady, non-circulatory force (Fung, 1993). Note also that (1) the acceleration reaction generates lift even when the wing is linearly accelerating along the horizontal plane (see the force traces in Dickinson and Götz, 1993) and that (2) the acceleration reaction is non-zero even when the wing is translating without linear acceleration but is rotating (due to the derivative of the rotational component of $v_{n(r,t)}$ in Equation 2).

Finally, the Magnus force due to Γ_M can be modeled by:

$$dF_{r(r,t)} = \tfrac{1}{4}\rho\pi c_{(r)}^2 \hat{r} R \dot{\alpha}_{(t)}^2 dR\,, \quad (14)$$

which is the product of the added mass ($\frac{1}{4}\rho\pi c_{(r)}^2 dR$), the translational velocity ($\hat{r}R\dot{\alpha}_{(t)}$) and the angular rotation ($\dot{\alpha}_{(t)}$) of the element (Fung, 1993; section 6.7, equation 10). Note that $dF_{r(r,t)}$ is a force arising from a circulatory component due to wing rotation but, unlike the unsteady circulatory force due to Γ_r, the Magnus force (due to Γ_M) is independent of both the angle of incident, α', and the rotational moment, $(\hat{x}_i - \hat{x}_{r(r)})c_{(r)}$. Except where noted, the Magnus force component is not included in the unsteady model.

Comparisons

Results from the USBE model are compared with both the measured forces on the dynamically scaled *Drosophila* wing (Dickinson et al., 1999) and the CFD-modeled forces on the virtual *Drosophila* wing (Sun and Tang, 2002). Wing chords for the physical wing were computed from an outline of the wing provided by M. H. Dickinson. Wing chords for the virtual wing were computed from the digitized outline of the illustrated wing in Sun and Tang (2002). For the comparisons with the virtual wing, the output forces were standardized by $\frac{1}{2}\rho S(\hat{r}_2 R\dot{\gamma})^2$. For the comparisons with the physical wing, the output forces were left unstandardized. Morphological and kinematic parameters for the three physical wing (PM1–PM3) and four virtual wing (VM1–VM4) comparisons are given in Table 1.

Results

Lift and drag for case PM1, the wing with unequal downstroke and upstroke $\alpha_{g(t)}$, are illustrated in Fig. 2. The shape of the unsteady drag curve is nearly identical to the measured drag curve, but the modeled peaks near the end of each stroke are approximately 20% greater than the measured peaks. The modeled drag during the translational phase of the

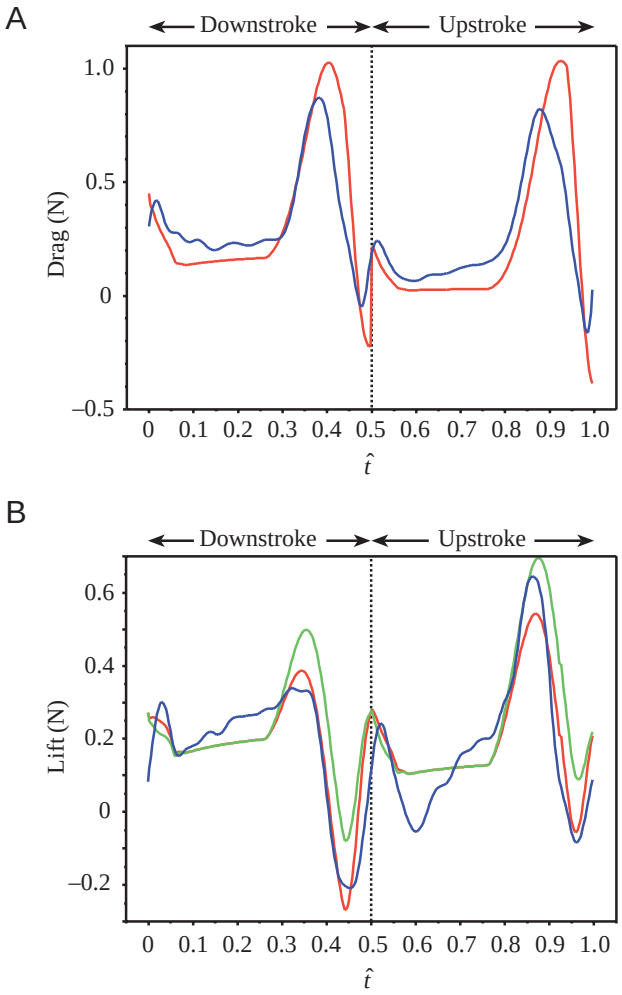

Fig. 2. Comparison of (A) drag and (B) lift across one stroke cycle for physical wing model 1 (PM1). The red line indicates the unsteady blade-element (USBE) model, the green line indicates the quasi-steady model with the Magnus force included, and the blue line indicates the measured forces on the physical wing model.

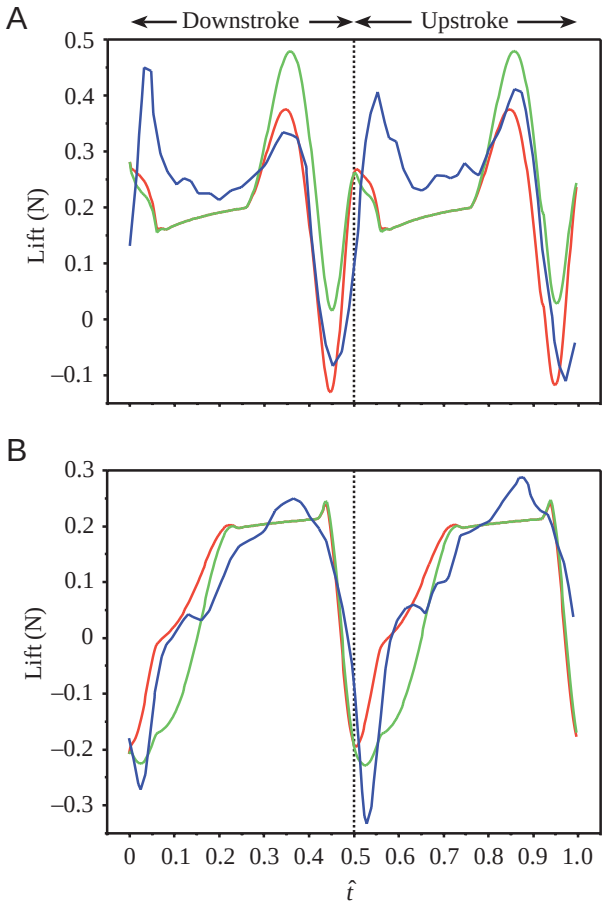

Fig. 3. Comparisons of lift across one stroke cycle for the (A) rotation-advance case (PM2) and (B) rotation-delayed case (PM3). The red line indicates the unsteady blade-element (USBE) model, the green line indicates the USBE model with the Magnus force included, and the blue line indicates the measured forces on the physical wing model.

upstroke is steady while the corresponding measured drag gradually rises. The modeled lift curve closely matches the measured lift curve, with the major differences occurring during the translation-only phase of the stroke cycle. Relative to the modeled rate, the measured rate of increased lift during the translation phase is slightly greater during the downstroke but much greater during the upstroke.

Both modeled and measured lift for case PM2 show distinct lift peaks at the beginning of each stroke, but the measured lift peaks are approximately 50% greater than the corresponding modeled lift peaks (Fig. 3). Similarly, the measured lift occurring during the translation phase of each stroke is distinctly greater than the modeled lift. By contrast, the magnitude of the modeled and measured lift peaks occurring at the ends of each stroke and the negative peaks occurring at stroke reversals are nearly identical. The general shape of the modeled and measured lift curves for case PM3 is very similar, but the broad lift peaks of the unsteady model are distinctly truncated, and the negative, measured peak at the downstroke–upstroke reversal is approximately 65% greater than the modeled peak.

VM1 and VM2 were used to demonstrate the effect of the duration of the linear acceleration phase, $\Delta\hat{\tau}_t$, on the presence of large force peaks at the beginning of each stroke (Sun and Tang, 2002). The similarity between the CFD-modeled and USBE-modeled curves is quite striking (Fig. 4). The magnitude of the rotation-dependent drag peak (the peak occurring at the beginning of the stroke) is approximately the same for the CFD and USBE curves, but the rotation-dependent lift peak is approximately 30% higher in the USBE curve. The USBE lift decomposition (Fig. 5) shows two important features. First, the end-stroke lift peak is dominated by the circulatory component, although a small acceleration reaction component does occur despite the fact that the wing is translating with zero acceleration during this part of the cycle. Second, the beginning-stroke lift peak is dominated by the acceleration reaction, as suggested previously (Sun and Tang, 2002).

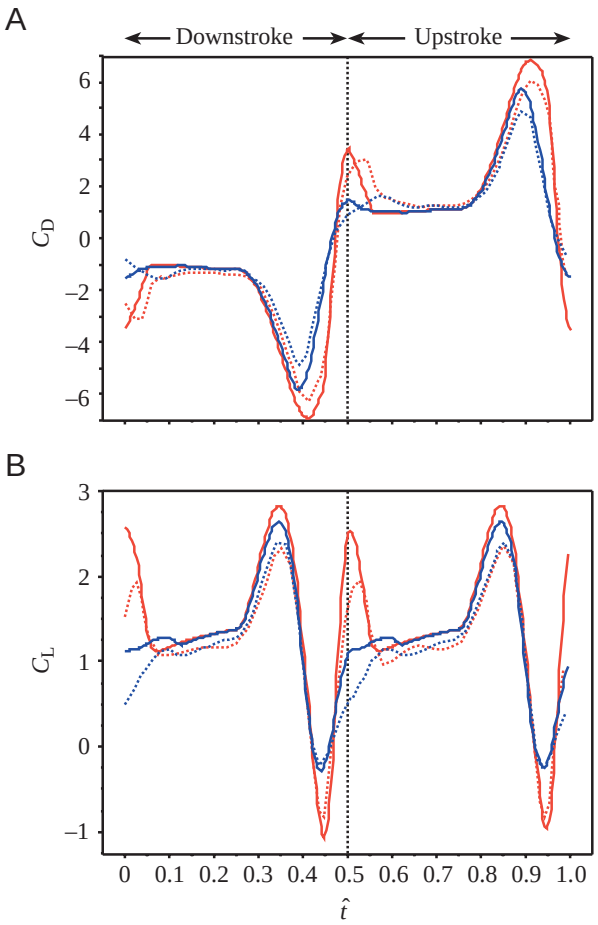

Fig. 4. Comparisons of (A) drag coefficient (C_D) and (B) lift coefficient (C_L) across one stroke cycle for virtual wing models VM1 and VM2. The unsteady blade-element (USBE) model results are shown with solid lines, while the computational fluid dynamic (CFD) model results are shown with broken lines. The low-magnitude, translational-acceleration case (VM1) is shown in blue. The high-magnitude, translational-acceleration case (VM2) is shown in red.

VM1, VM3 and VM4 were used to demonstrate the effect of the timing of wing rotation relative to stroke reversal (Sun and Tang, 2002), and the general features of the lift curve are similar to the corresponding physical wing experiments (Dickinson et al., 1999). Again, the similarity of the CFD-modeled and USBE-modeled curves is remarkable (Fig. 6). The drag curves differ in one important respect: the CFD-delayed curve presents a distinct peak at the beginning of each stroke that is nearly twice the magnitude of the corresponding peak in the USBE model. The CFD and USBE lift curves for VM3 and VM4 show differences that occur in VM1 but are greatly magnified. In other words, while the USBE estimates of lift during the translation phase are approximately 0.1 units higher than the CFD estimates for VM1, this difference is 0.25 units higher for VM3 and VM4. Importantly, however, the slope of the lift curve during the translation phase is nearly identical for the CFD and USBE models.

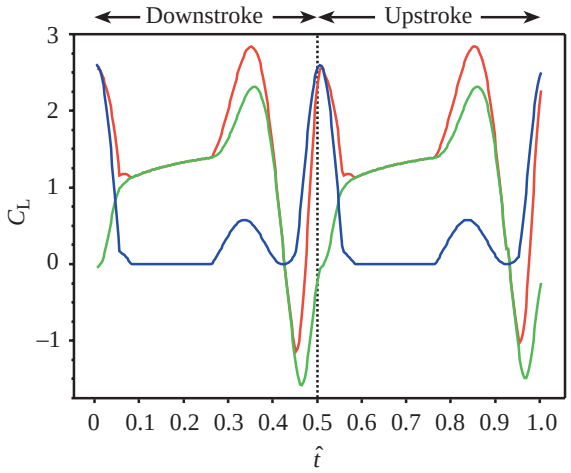

Fig. 5. Decomposition of the unsteady blade-element (USBE) model (red line) of VM2 into circulatory (green) and added mass (blue) components. C_L, lift coefficient.

The addition of the Magnus force to the unsteady model has no effect on drag because of the horizontal stroke plane. Except for perhaps PM3, the addition of the Magnus force to the unsteady model results in a generally worse fit to the measured results because of the more positive peaks during wing rotation (Figs 1, 2). These results suggest that the influence of the Magnus force is trivial, at best, during the hovering flight of *Drosophila*. Because of the generally worse fit when the Magnus force is included in the unsteady model, its effect was removed for all comparisons with the virtual wing model.

Discussion

Accuracy of the unsteady model

The subtle kinematic changes exploited by animals to control swimming and flying forces are not well known (Taylor, 2001). The map of variation in measured forces on a pair of motor-driven wings as a function of wing kinematics provides detailed predictions on how animals might control locomotor forces (Sane and Dickinson, 2001). Comparisons of limb kinematics and body forces on tethered animals allow detailed investigation of locomotor control, but the tethering may introduce artifacts that are not found in freely flying animals. Ultimately, we want to know how freely moving animals control locomotor forces, a goal that will require a comparison of detailed limb kinematics and body dynamics.

Such comparisons are uncommon. The pectoral fin kinematics during the flapping flight of the bird wrasse *Gomphosus varius* were compared with measures of instantaneous dorsoventral and anteroposterior accelerations of the body in order to infer control of swimming forces (Walker and Westneat, 1997). Measures of body dynamics in freely moving animals require the numerical differentiation of the measured displacement of the body with respect to time. The errors involved in this type of analysis have been discussed previously (Harper and Blake, 1989; Walker, 1998).

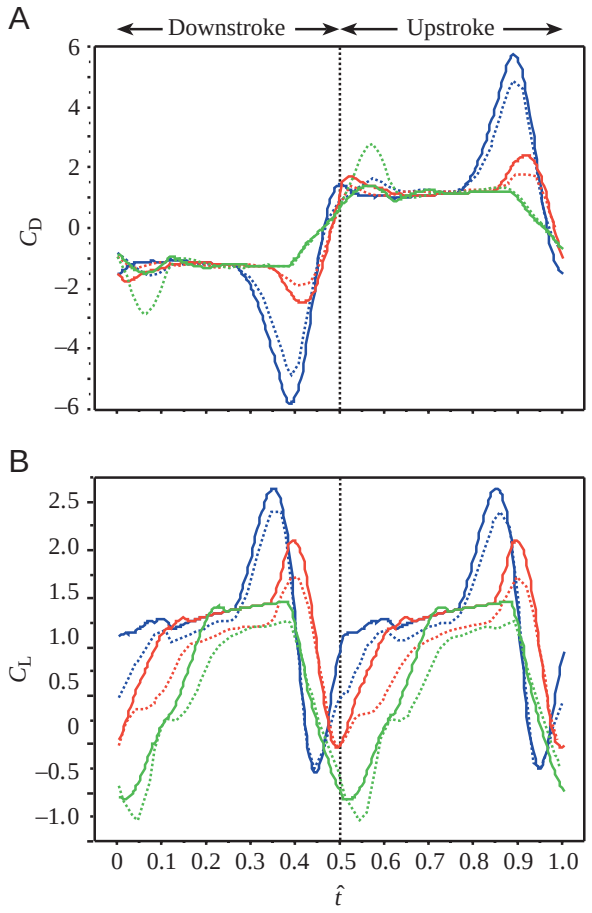

Fig. 6. Comparisons of (A) drag coefficient (C_D) and (B) lift coefficient (C_L) across one stroke cycle for VM1, VM3 and VM4. The unsteady blade-element (USBE) model results are shown with solid lines, while the computational fluid dynamic (CFD) model results are shown with broken lines. The rotation-advanced case (VM1) is shown in red, the symmetric case (VM3) is shown in blue, and the rotation-delayed case (VM4) is shown in green.

A complimentary approach to estimating body dynamics with a numerical differentiation method is the application of a fluid-dynamic model to the limb kinematics. The USBE model explored in the present study was initially developed to compare the performance of oscillating limbs undergoing a variety of motions at Reynolds numbers (*Re*) above 1000 (Walker and Westneat, 2000) and below 100 (Walker, 2002). The results of the present study suggest that predictions from the simulations are probably robust against small errors in the unsteady model. The application of the unsteady model to the investigation of locomotor control in freely moving animals should also require reasonable model accuracy. While the ability of the unsteady model to estimate measured forces on motor-driven plates was briefly discussed previously (Walker and Westneat, 2000), it is worth checking the accuracy of the model more formally. The comparison of the unsteady results to the measured forces on the physical model (Dickinson et al., 1999) with the CFD results on the virtual model allows this comparison (Sun and Tang, 2002).

In general, the shape and elevation of the force curves from the USBE model are quite similar to the corresponding physical model and CFD curves. The slopes of the USBE drag and, especially, lift curves during the translation phases differ from those of the physical model curves but are strikingly similar to the slopes seen in the CFD model curves. Although the slopes during the translation phase are similar for the USBE and CFD models, the USBE lift estimates are consistently 12–18% greater than the CFD estimates. Indeed, the USBE estimate of the mean lift coefficient $\bar{C}_L$ across the whole stroke cycle ranges from 6% to 25% greater than the CFD estimate (similar trends occur with the drag coefficient C_D but, because of the larger scale, these trends are only conspicuous during the rotational peaks). The relationship between the USBE and physical model during the translation phase is more variable, largely because of the variability in the measured forces. The source of this variability is unknown but is clearly not being accounted by either the unsteady or CFD models.

While the USBE model captures the rotation-dependent force peaks effectively (e.g. at the end of the strokes in Figs 2, 3), it fails to capture the rotation-independent peaks when these are large (e.g. at the beginning of each stroke in Fig. 3). While the modeled peaks reflect an inertial contribution (acceleration reaction) to the force balance (Fig. 5), this mechanism is clearly insufficient to account for the large measured peaks. These results, then, support the original interpretation that these peaks reflect wake capture (Dickinson et al., 1999) and not the acceleration reaction (Sun and Tang, 2002).

The similarity between the USBE model results and the physical and, especially, CFD model results suggests that, with few caveats, the USBE model is sufficient to investigate both simulated kinematic parameter spaces (Walker and Westneat, 2000; Walker, 2002) and locomotor control from measured kinematic variables in freely moving animals. The principal caveats of the broad application of the model are accounting for the effects of reduced frequency, *Re* and model wing shape on the measured force coefficients. Unfortunately, there is no work measuring the force coefficients on root-oscillating wings with finite reduced frequencies (i.e. in translation). The lift and drag coefficients employed in this study reflect the influence of the induced downwash, which influence should decrease as the reduced frequency approaches zero. To account for this decreased influence, one could use two-dimensional coefficients and apply a model of the induced downwash (DeLaurier, 1993; Kamakoti et al., 2000; Hedrick et al., 2002) to the estimate of α'. Two-dimensional force coefficients on root-oscillating wings across a range of attack angles have not been published, but the two-dimensional coefficients at α'=45° are 8% greater than the three-dimensional coefficients (Birch and Dickinson, 2001).

The effects of scale have not been measured on root-oscillating wings at low *Re* (<100), although two-dimensional results on static airfoils predict a large *Re* effect (Thom and Swart, 1940). Experiments with the *Drosophila* wing model show that force coefficients are stable for *Re* between 100 and 1000 (Sane and Dickinson, 2002). More surprisingly, only small

differences in C_D and, especially, C_L were found for a series of real and model wings tested at *Re* between 1100 and 26 000 (Usherwood and Ellington, 2002b). With a more systematic study of *Re* effects on wing performance, even this small *Re* influence can be easily incorporated into the USBE model.

Both wing aspect ratio and the distribution of wing area might influence wing performance, but the effects of wing-area distribution have not been investigated. Wing aspect ratio has only a very small effect on C_L at all α', but the C_D of lower aspect ratio wings increases more rapidly than that of higher aspect ratio wings as α' increases (Usherwood and Ellington, 2002b). These results suggest that wing shape effects should be more systematically explored and incorporated into future studies with the USBE model.

Comparison with a rotational-coefficient model

The theoretical lift coefficient, $C_L=2\pi\alpha'$, on a wing section at a low angle of incidence is derived from a simple algebraic rearrangement of:

$$\rho U(\Gamma_t+\Gamma_h+\Gamma_r)\approx\tfrac{1}{2}\rho cU^2C_L\,. \qquad (15)$$

Indeed, the small incident angle assumption reduces Equations 2 and 3 to the more familiar equations given in Fung (1993) or Zbikowski (2002). For higher angles of incidence, the results presented here suggest that empirically derived coefficients as a function of α' result in good predictions of measured forces. An alternative to estimating a single coefficient as a function of all three kinematic components would be to compute a separate coefficient for each kinematic component. Indeed, a quasi-steady model of hovering flight in *D. melanogaster* using separate heave and rotational force coefficients was developed recently (Sane and Dickinson, 2002). Rotational force coefficients were computed by standardizing the estimated rotational force component, which is the residual force remaining after subtracting the quasi-steady translational force (the quasi-steady force estimated using only the translational component of v_n) from the measured force at a point in the stroke cycle when inertial forces are trivial. The lift for cases PM2 and PM3 estimated by the USBE model and the rotational-coefficient quasi-steady (RCQS) model were compared. For the RCQS model, rotational coefficients, which are a function of both $\hat{x}_0$ and the non-dimensional angular velocity, $\hat{\omega}=\dot{\alpha}\bar{c}/\dot{\gamma}R$ (Sane and Dickinson, 2002), were computed using a linear interpolation between the coefficients estimated from the regression parameters for the pair of $\hat{\omega}$ in table 1 of Sane and Dickinson (2002) that bounded the instantaneous $\hat{\omega}$. The close match between the USBE and RCQS curves (Fig. 7) suggests that the empirically derived rotational force coefficients do not reflect a contribution from the Magnus circulation, Γ_M. Instead, the close match simply indicates that the USBE and RCQS models are simply alternative methods for incorporating the effects of Γ_r into a semi-empirical blade-element model.

Rotational lift: something different or more of the same?

The rotation-dependent force that has been compared to the Magnus effect is quantitatively explained by a model of the same circulatory-and-attached-vortex force that also dominates the force balance during wing translation. Indeed, if Magnus forces are included in the model, the predicted lift and drag peaks are much larger than the corresponding peaks estimated from the physical wing or virtual wing (CFD) models. A recent CFD flow reconstruction clearly shows the attached vortex throughout the rotational phase (Sun and Tang, 2002). It is, therefore, not surprising that the unsteady coefficients (Dickinson et al., 1999), which reflect the augmenting effects of an attached vortex on a translating wing, can explain the forces occurring during wing rotation.

Why do previous quasi-steady models (with the exception of the RCQS model of Sane and Dickinson, 2002) fail to capture the magnitude of the rotation-dependent force? Both the quasi-steady force of Sun and Tang (2002) and the quasi-steady translational forces of Dickinson et al. (Dickinson et al., 1999; Sane and Dickinson, 2001, 2002) are modeled as a function of the angle of the chord relative to the stroke plane,

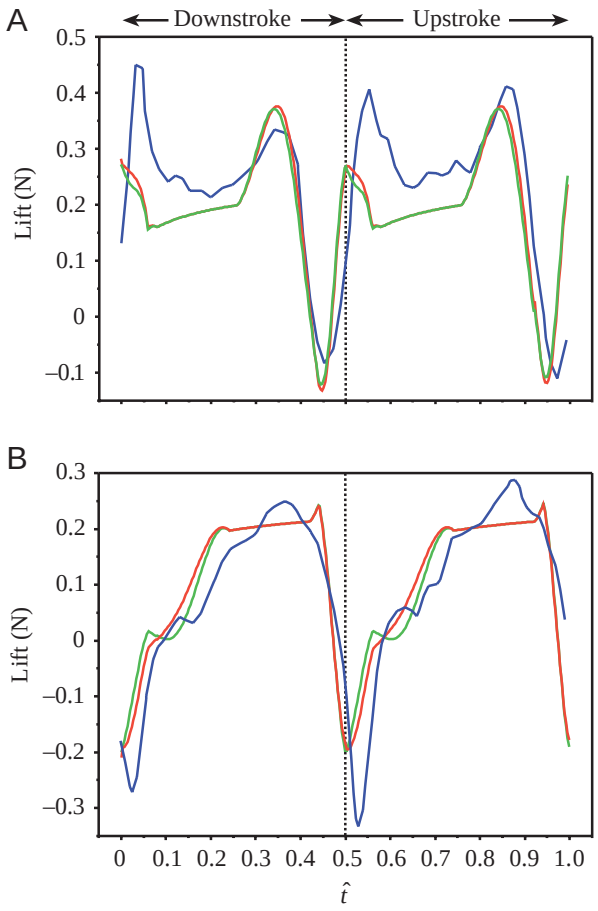

Fig. 7. Comparisons of lift for cases (A) PM2 and (B) PM3 estimated by the unsteady blade-element (USBE) model (red line) and a quasi-steady model that separately estimates a translational circulatory force and a rotational circulatory force using rotational coefficients (green line). The measured forces (blue line) are shown for comparison.

which is horizontal in a hovering *Drosophila*. The incident flow vector, therefore, was modeled by both groups as if the wing was not rotating. Indeed, the quasi-steady model of Sun and Tang (2002) did not account for the changing angle of the wing chord during rotation. But, as shown above, the incident flow vector and corresponding α' and circulatory force are a function of the tangential velocity (due to rotation) of the chordwise center of incident flow relative to the chordwise center of rotation in addition to the translational velocity. By accounting for this rotational component to the incident flow, the USBE model can explain the rotation-dependent forces occurring during wing rotation.

Comparisons of the rotation-dependent force component with the Magnus effect, then, are misleading. While the behavior of the rotation-dependent force component partially resembles the Magnus effect, this behavior results from the distortion of the boundary layer due to the changing geometry of the incident flow and, therefore, the mechanism precisely resembles that of a pitched wing in a uniform flow. This interpretation of the rotation-dependent force peak occurring during wing rotation suggests that rotational lift is not a novel aerodynamic mechanism but is a consequence of a kinematic mechanism that augments incident-angle-dependent circulation and the resulting circulatory-and-attached-vortex force. Finally, this kinematic mechanism has interesting but unexplored implications for the evolution of wing shape, as the magnitude of the vortex force occurring during wing rotation is a function of $\hat{x}_{r(r)}c_{(r)}$.

List of symbols

$\bar{C}_L$	mean lift coefficient
$C_{L(r,t)}$	lift coefficient of wing element
$C_{D(r,t)}$	drag coefficient of wing element
$c_{(r)}$	chord length
$\bar{c}$	mean chord
$dD'_{(r,t)}$	circulatory drag
$dD_{a(r,t)}$	aft component of added mass force
$dD_{c(r,t)}$	aft component of circulatory force
$dF_{a(r,t)}$	added mass force
$dF_{n(r,t)}$	normal component of circulatory force
$dF_{r(r,t)}$	Magnus force
$dF_{x(r,t)}$	chordwise component of circulatory force
$dL'_{(r,t)}$	circulatory lift
$dL_{a(r,t)}$	upward component of added mass force
$dL_{c(r,t)}$	upward component of circulatory force
dR	wing element span
$\dot{h}_{(r,t)}$	heaving velocity
R	wing length
r	radial position along wing span
$\hat{r}$	non-dimensional radial position along wing span
S	wing area
t	time
$\hat{t}$	standardized time
U	fluid velocity
$v_{n(r,t)}$	normal velocity of wing element
$v_{(r,t)}$	velocity of wing element
$v_{x(r,t)}$	chordwise velocity of wing element
$\dot{v}_n$	first derivative of normal velocity of wing element
$\hat{x}_o$	rotational axis
$\hat{x}_i$	non-dimensional chordwise location of center of incident flow
$\hat{x}_{r(r)}$	non-dimensional chordwise location of center of rotation
$\alpha_{(t)}$	wing pitch
$\alpha_{g(t)}$	geometric angle of attack
$\alpha'_{(r,t)}$	angle of incidence
β_n	added mass coefficient
$\Phi_{(r,t)}$	Wagner function
$\gamma_{(t)}$	azimuth position of wing
ρ	fluid density
$\hat{\tau}_f$	non-dimensional rotational timing parameter
$\Delta\hat{\tau}_r$	non-dimensional duration of wing rotation
$\Delta\hat{\tau}_t$	non-dimensional duration of wing translational acceleration
Γ_t	translational circulation
Γ_h	heaving circulation
Γ_r	rotational circulation
Γ_M	Magnus circulation
$\hat{\omega}$	non-dimensional angular velocity

I would like to extend special thanks to M. H. Dickinson and S. Sane for their time and patience with my work on modeling *Drosophila* hovering. I also thank two anonymous reviewers for greatly improving the clarity of this manuscript. This work was supported by ONR (N00014-01-1-0506), NSF (IBN-0119643) and the Bioscience Research Institute of Southern Maine.

References

Birch, J. M. and Dickinson, M. H. (2001). Spanwise flow and the attachment of the leading-edge vortex on insect wings. *Nature* **412**, 729-733.

DeLaurier, J. D. (1993). An aerodynamic model for flapping-wing flight. *Aeronaut. J.* **97**, 125-130.

Dickinson, M. H. and Götz, K. G. (1993). Unsteady aerodynamic performance of model wings at low Reynolds numbers. *J. Exp. Biol.* **174**, 45-64.

Dickinson, M. H., Lehmann, F.-O. and Sane, S. P. (1999). Wing rotation and the aerodynamic basis of insect flight. *Science* **284**, 1954-1960.

Ellington, C. P. (1984). The aerodynamics of hovering insect flight. IV. Aerodynamic mechanisms. *Phil. Trans. R. Soc. Lond. B* **305**, 79-113.

Fung, Y. C. (1993). *An Introduction to the Theory of Aeroelasticity.* New York: Dover.

Harper, D. G. and Blake, R. W. (1989). A critical analysis of the use of high-speed film to determine maximum accelerations of fish. *J. Exp. Biol.* **142**, 465-471.

Hedrick, T. L., Tobalske, B. W. and Biewener, A. A. (2002). Estimates of circulation and gait change based on a three-dimensional kinematic analysis of flight in cockatiels (*Nymphicus hollandicus*) and ringed turtle-doves (*Streptopelia risoria*). *J. Exp. Biol.* **205**, 1389-1409.

Kamakoti, R., Berg, M., Ljungqvist, D. and Shyy, W. (2000). A computational study for biological flapping wing flight. *Trans. Aero. Astro. Soc. China* **32**, 265-279.

Kuethe, A. M. and Chow, C.-Y. (1986). *Foundations of Aerodynamics.* New York: John Wiley & Sons.

Sane, S. and Dickinson, M. H. (2001). The control of flight force by a flapping wing: lift and drag production. *J. Exp. Biol.* **204**, 2607-2626.

Sane, S. and Dickinson, M. H. (2002). The aerodynamic effects of wing rotation and a revised quasi-steady model of flapping flight. *J. Exp. Biol.* **205**, 1087-1096.

Sun, M. and Tang, J. (2002). Unsteady aerodynamic force generation by a model fruit fly wing in flapping motion. *J. Exp. Biol.* **205**, 55-70.

Taylor, G. K. (2001). Mechanics and aerodynamics of insect fight control. *Biol. Rev.* **76**, 449-471.

Theodorsen, T. (1935). General theory of aerodynamic instability and the mechanism of flutter. *NACA Report 496*.

Thom, A. and Swart, P. (1940). Forces on an airfoil at very low speeds. *J. Roy. Aero. Soc.* **44**, 761-770.

Usherwood, J. R. and Ellington, C. P. (2002a). The aerodynamics of revolving wings. I. Model hawkmoth wings. *J. Exp. Biol.* **205**, 1547-1564.

Usherwood, J. R. and Ellington, C. P. (2002b). The aerodynamics of revolving wings. II. Propeller force coefficients from mayfly to quail. *J. Exp. Biol.* **205**, 1565-1576.

Van den Berg, C. and Ellington, C. P. (1997a). The three-dimensional leading-edge vortex of a 'hovering' model hawkmoth. *Phil. Trans. R. Soc. Lond. B* **352**, 329-340.

Van den Berg, C. and Ellington, C. P. (1997b). The vortex wake of a 'hovering' model hawkmoth. *Phil. Trans. R. Soc. Lond. B* **352**, 317-328.

Walker, J. A. (1998). Estimating velocities and accelerations of animal locomotion: A simulation experiment comparing numerical differentiation algorithms. *J. Exp. Biol.* **201**, 981-995.

Walker, J. A. (2002). Functional morphology and virtual models: Physical constraints on the design of oscillating wings, fins, legs, and feet at intermediate Reynolds numbers. *Int. Comp. Biol.* **42**, 232-242.

Walker, J. A. and Westneat, M. W. (1997). Labriform propulsion in fishes: Kinematics of flapping aquatic flight in the bird wrasse *Gomphosus varius* (Labridae). *J. Exp. Biol.* **200**, 1549-1569.

Walker, J. A. and Westneat, M. W. (2000). Mechanical performance of aquatic rowing and flying. *Proc. R. Soc. Lond. B* **267**, 1875-1881.

Zbikowski, R. (2002). On aerodynamic modelling of an insect-like flapping wing in hover for micro-air vehicles. *Phil. Trans. R. Soc. Lond. A* **360**, 273-290.